

# OAFuser: Towards Omni-Aperture Fusion for Light Field Semantic Segmentation

Fei Teng\*, Jiaming Zhang\*, Kunyu Peng, Yaonan Wang, Rainer Stiefelhagen, and Kailun Yang†

**Abstract**—Light field cameras, by harnessing the power of micro-lens array, are capable of capturing intricate angular and spatial details. This allows for acquiring complex light patterns and details from multiple angles, significantly enhancing the precision of image semantic segmentation, a critical aspect of scene interpretation in vision intelligence. However, the extensive angular information of light field cameras contains a large amount of redundant data, which is overwhelming for the limited hardware resources of intelligent vehicles. Besides, inappropriate compression leads to information corruption and data loss. To excavate representative information, we propose a new paradigm, *Omni-Aperture Fusion model (OAFuser)*, which leverages dense context from the central view and discovers the angular information from sub-aperture images to generate a semantically consistent result. To avoid feature loss during network propagation and simultaneously streamline the redundant information from the light field camera, we present a simple yet very effective *Sub-Aperture Fusion Module (SAFM)* to embed sub-aperture images into angular features without any additional memory cost. Furthermore, to address the mismatched spatial information across viewpoints, we present a *Center Angular Rectification Module (CARM)* to realize feature resorting and prevent feature occlusion caused by asymmetric information. Our proposed OAFuser achieves state-of-the-art performance on the UrbanLF-Real and -Syn datasets and sets a new record of 84.93% in mIoU on the UrbanLF-Real Extended dataset, with a gain of +4.53%. The source code of OAFuser will be available at <https://github.com/FeiBryantkit/OAFuser>.

**Impact Statement**—Recently, to enhance scene understanding tasks, multiple works have introduced depth or thermal information. Inspired by these works, few attempts have implemented semantic segmentation based on light field cameras, which provide both spatial information (RGB image) and angular information (image array along angular coordinates). However, the abundance of information simultaneously restricts the application of light field cameras in dense predictive tasks. In light of this, we propose a pioneering and effective framework that addresses the issue of increasing memory costs as the number of sub-aperture images grows. This has practical value for the exploration and application of light field cameras. The proposed method provides a scalable solution for scene parsing tasks based on light field cameras. This may inspire more members of the community to

This work was supported in part by the Ministry of Science, Research and the Arts of Baden-Württemberg (MWK) through the Cooperative Graduate School Accessibility through AI-based Assistive Technology (KATE) under Grant BW6-03, in part by the University of Excellence through the “KIT Future Fields” project, in part by the Helmholtz Association Initiative and Networking Fund on the HAICORE@KIT partition, and in part by Hangzhou SurImage Technology Company Ltd.

F. Teng, Y. Wang, and K. Yang are with the School of Robotics and the National Engineering Research Center of Robot Visual Perception and Control Technology, Hunan University, Changsha 410082, China.

J. Zhang, K. Peng, and R. Stiefelhagen are with the Institute for Anthropomatics and Robotics, Karlsruhe Institute of Technology, 76131 Karlsruhe, Germany.

\*Equal contribution.

†Corresponding author (E-Mail: kailun.yang@hnu.edu.cn.).

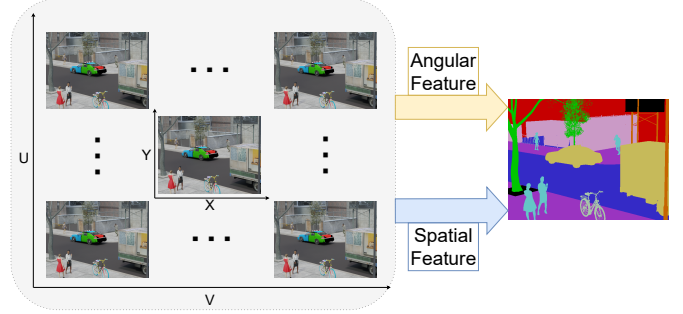


Fig. 1: A light field camera captures a more comprehensive range of spatial and angular information, contributing to pixel-wise image segmentation. The fusion of omni-aperture features enhances urban semantic scene understanding.

pay attention to and develop light field cameras.

**Index Terms**—Semantic segmentation, light field, scene parsing, vision transformers, scene understanding.

## I. INTRODUCTION

**I**NTELLIGENT agents, such as robotics and autonomous driving systems, heavily rely on visual understanding tasks, especially image semantic segmentation, which can produce pixel-level prediction results and contribute to determining the category, shape, and position of objects [1], [2], [3]. To effectively apply semantic segmentation in real-world scenarios, *accuracy* is one of the most crucial factors. To enhance the accuracy, advanced models, such as ConvNets [4], [5] and MLP-based methods [6], and attention mechanism [7], [8], are introduced. Furthermore, different fusion strategies for segmentation [9], [10], [11], [12] are proposed to improve the perception ability.

In this work, we introduced Light Field (LF) cameras [13]. These cameras are equipped with a unique optical system, referred to as an “omni-aperture”, which indicates their ability to utilize all available apertures to capture comprehensive light information. They record the volumetric radiance of a scene, surpassing the capabilities of traditional photography by capturing more complex data, which includes information beyond the standard two-dimensional plane. Specifically, LF cameras retain details about the angle of incoming light rays, effectively capturing four-dimensional light-field data. For autonomous driving, the ability of LF cameras to simultaneously capture spatial information from multiple directions allows for a more nuanced understanding of the driving environment. The variations captured between the central and sub-aperture

Method	Hardware Demand and Extra Efforts			The Capacity of the Network		
	#Modality	Memory Cost	Independent of Depth Map	Angular Information	Feature Rectification	Independent of Image Quality
RGB Based Network	1	n.a.	n.a.	✗	✗	✗
RGB-D based Network	2	n.a.	✗	✗	✓	✗
OCR-LF [16]	More than 2	✗	✓	✓	✗	✗
PSPNet-LF [16]	More than 2	✗	✓	✓	✗	✗
LF-IENet [19]	More than 2	✗	Explicit	Implicit	✗	✗
OAFuser (ours)	<b>Flexible</b>	✓	✓	✓	✓	✓

TABLE I: Challenges of light field semantic segmentation. The *#Modality* indicates the number of sub-aperture images used. In the *Memory Cost*, *n.a.* denotes that the memory cost also increases with an increase in the number of images. *Independent of Depth Map* indicates whether depth information is required. *Angular Information* column describes the utilization of angular information. Finally, the *Independent of Image Quality* indicates the issue of out-of-focused images from light field cameras. As for LF-IENet, *Disparity Map* is explicitly generated, and *Angular Information* is hidden in the implicit branch.

images provide rich visual details, especially beneficial for identifying geometrically complex regions. By harnessing both the spatial and angular data, LF technology can facilitate shifting focus across different planes after the fact, enabling refined visual computations critical for dense vision tasks such as those required in robotics vision perception [14].

Despite the theoretical benefits, we observe two under-explored challenges of applying LF cameras in scenes semantic segmentation task, as presented in Table I: (1) high demands on hardware and data processing; (2) effective use of angular features. In this work, we propose a novel **Omni-Aperture Fusion (OAFuser)** model to address those challenges above, thereby contributing to the community.

First, high memory costs for redundant sub-aperture information and extra efforts related to complex data pre-processing are required to handle LF-based semantic segmentation. For example, assigning a feature extractor to each LF image can over-burden the device. Especially, using an LF camera with a spatial resolution of  $640 \times 480$  and angular resolution of  $9 \times 9$  will bring a macro-pixel image with  $4320 \times 5760$ , imposing 81 times of data stream along the network module. However, compressing LF images into a depth map [15], [16] will additionally increase the complexity of the model. Moreover, the quality of the generated depth map [17], [18] directly impacts the segmentation performance. To overcome these issues and explore the efficiency of using LF cameras without the need for additional hardware or architectural modifications, we propose a simple yet effective **Sub-Aperture Fusion Module (SAFM)** that allows our OAFuser network to utilize an arbitrary number of sub-aperture images, so as to achieve efficient semantic segmentation without additional memory cost. Especially, the SAFM can distinguish the primary and interfering features channel-wise by analyzing the image features from different viewpoints. Besides, rich information from LF images is embedded into angular feature maps and spatial feature maps and further fed into respective transformer blocks. Thanks to the SAFM module, our OAFuser network can achieve better performance while avoiding excessive memory costs.

Second, the ability of the network regards the performance, *i.e.*, angular feature expression and asymmetric feature rectification. Previous methods introduce a sub-optimal solution for the LF image representation. While stacking images into an array [16], [18] contains solely one-dimensional angular

information, converting into a video sequence [20], [21] ignores the implicit angular relationship of LF images. Besides, direct merging images or features results in blurred or mixed boundaries, and this phenomenon is particularly severe with the increase of sub-aperture images. However, the single sub-aperture image captured by certain micro-lenses contains much noise [22], [23]. Moreover, the initial LF images are not entirely focused, which can exacerbate this issue. In this work, we introduce a **Center Angular Rectification Module (CARM)** to perform effective rectification between the center view and the aperture-based features. Apart from other strategies in which the features are directly fused with others, our network adopts iteration feature rectification to incorporate the asymmetric angular feature and spatial features from the SAFM before the fusion stage, as shown in Fig. 2. This design allows the OAFuser network to explore the relationship between different features and has realigned the angular and spatial information, further contributing to the segmentation task.

To demonstrate the effectiveness of the proposed OAFuser architecture, we conduct a comprehensive variety of experiments on different LF semantic segmentation datasets. On the UrbanLF-Real dataset, OAFuser achieves 82.69% in mIoU with an increase of +3.37%. On the UrbanLF-Syn dataset, OAFuser surpasses previous works and attains 81.93% in mIoU. Compared to previous state-of-the-art methods, OAFuser reaches the best mIoU of 84.93% with a notable mIoU improvement of +4.53% on the UrbanLF-RealE dataset, while no additional parameters are required.

At a glance, we deliver the following contributions:

- We propose a novel paradigm, Omni-Aperture Fusion model, *i.e.*, **OAFuser**, to perform LF semantic segmentation leveraging the structural characteristics of LF cameras, which addresses crucial challenges and enables the handling of an arbitrary number of sub-aperture images.
- We design a **Sub-Aperture Fusion Module (SAFM)** to fuse and embed rich angular information from highly redundant representation, and a **Center Angular Rectification Module (CARM)** to match and rectify information imbalances caused by variations from different angles.
- We verify our method through extensive experiments on three datasets, *i.e.*, UrbanLF-Real, UrbanLF-Syn, and UrbanLF-RealE, which is a real-world dataset with ex-

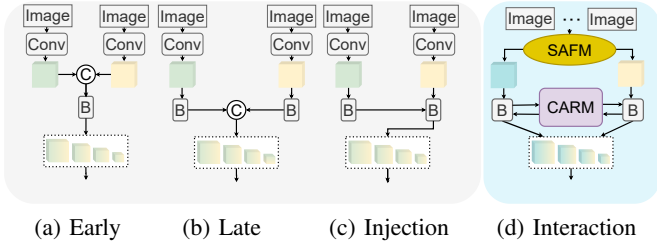


Fig. 2: **Paradigms of LF semantic segmentation model.** Compared to conventional fusion methods, our interaction fusion can handle an arbitrary number of LF images, and the features from different branches interact with each other.

tended synthetic samples.

## II. RELATED WORK

In this section, the overview of semantic segmentation is introduced in Sec. II-A, while our work is a pixel-level classification task for urban scenes. Since the enormous and asymmetric image representation from different microlens of the LF camera, various multi-modal semantic segmentation works are presented in Sec. II-B. Furthermore, to boost the angular information expression and better use the asymmetric information of LF cameras, several applications for LF cameras that have given us a great deal of inspiration are also thoroughly introduced. in Sec. II-C.

### A. Semantic Segmentation

Semantic scene segmentation, as a fundamental task of computer vision, plays a crucial role in scene understanding tasks, such as autonomous driving and intelligent transportation systems [24], [25], by assigning a category to each pixel. Since FCN [26] pioneers the use of convolutional neural networks to replace fully connected networks to propose an end-to-end framework, many segmentation works have emerged based on this approach, and the efficiency and accuracy of segmentation have been vastly improved. For instance, [27], [28] adopt an encoder-decoder structure to capture contextual information and local details. Then, [27], [29] introduce dilated convolution to increase the receptive field. To enhance the global context representation, [30], [31] adopt a pyramidal hierarchy in the encoding path. Furthermore, enhancing prior contextual information [32], [33], [34] contributes to improving segmentation results. Since the introduction of the self-attention mechanism in vision tasks [35], many following works [7], [8], [25] propose dense prediction, attention-based models. Meanwhile, some other works introduce lightweight backbones to speed up the inference [36], [37], [38].

Although those studies demonstrate excellent results in handling dense prediction tasks, they still suffer from limitations in image quality, leading to performance degradation in handling complete areas, such as shallow or out-of-focus areas in real-world driving scene understanding scenarios. LF cameras, unlike monocular cameras, are equipped with an omni-aperture feature. Therefore, focusing on monocular RGB semantic segmentation that emphasizes single-image spatial

features fails to utilize the angular information provided by LF cameras. Additionally, the sub-aperture images produced by these cameras contain a significant amount of noise.

### B. Multi-Modal Semantic Segmentation

The multiple sub-aperture images captured by the LF camera can be considered as various RGB modalities with inherent relationships. Therefore, the research on multi-modal semantic segmentation is essential for exploring the potential of LF cameras. ACNet [39] and EDCNet [40] leverage attention connections for facilitating cross-modal interactions in RGB-Depth and RGB-Event semantic segmentation, respectively. MMFNet [41] enables the fusion of multiple medical images by aggregating different features in spatial and channel domains. NestedFormer [42] proposed a feature aggregation module to fulfill multi-modal medical image segmentation. Furthermore, ESANet [43] and SA-Gate [15] utilize depth maps and RGB images to achieve high-accuracy semantic segmentation by employing uniquely designed fusion modules. PGSNet [44], which introduces a dynamic integration module, achieves glass segmentation. Additionally, [45], [46], [47] adopt RGB-thermal image fusion. Significantly, the works of CMX [12], [48] present an arbitrary-modal fusion network, which can handle RGB and any other modality, such as depth, thermal, polarization, event, or LiDAR data. HRFuser [49] realizes the fusion of an arbitrary number of additional modalities as supplementary information into RGB images by introducing multi-window cross-attention.

However, these methods, which are focused on handling symmetrical modalities, are not suitable for pixel-wise prediction tasks in LF images. This is because the pixel shifting between different sub-aperture images caused by micro-lenses can adversely affect semantic segmentation results. Our proposed OAFuser concentrates on utilizing the diverse angular information in LF images and considers the mismatching from images captured by all sub-apertures of LF cameras.

### C. Light Field Scene Understanding

Traditional cameras require the focal length to be set in advance during shooting. However, with LF cameras, users can adjust the focus point and refocus after capturing, meaning users can decide which part of the image is sharp and which part is blurred after the shot [50], [51]. Due to their rich visual information, LF cameras have found wide applications in various areas, such as saliency detection [52], [53], depth estimation [54], [55], and super resolution [56], [57]. Meanwhile, research in other related communities is crucial to our work, as light-field cameras are still an under-explored area in the vision community.

FES [58] achieves sub-aperture feature fusion via spatial and channel attention. NoiseLF [59] utilizes the all-focus central-view image and its corresponding focal stack, with a unique-designed forgetting matrix and confidence re-weighting strategy, to achieve supervised saliency detection under noisy labels. Furthermore, several works [60], [61], [62] employ sub-aperture images, macro-pixel images, epipolar images, or

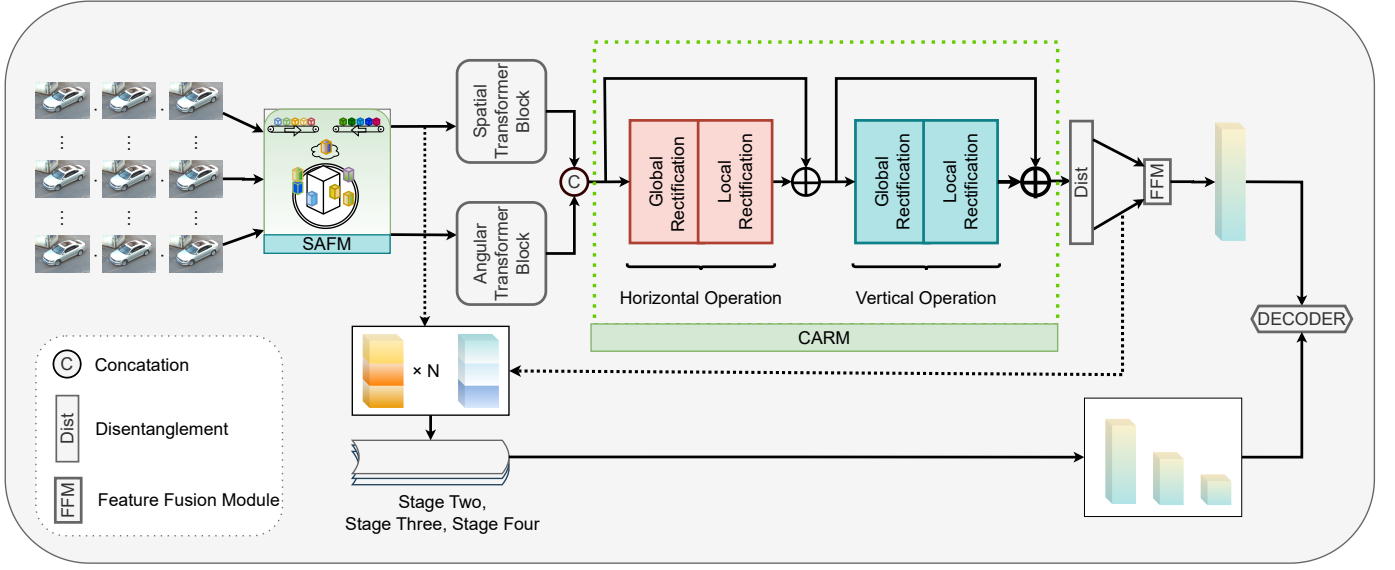


Fig. 3: Overall structure of the OAFuser model for omniper-aperture fusion. An arbitrary number of sub-aperture images is fed into the model. The *Sub-Aperture Fusion Module (SAFM)* in Sec. III-B generates both angular feature and spatial feature. The *Horizontal Operation* and *Vertical Operation* of *Center Aperture Rectification Module (CARM)* in Sec. III-C are implemented for asymmetric feature rectification. Afterward, the four-stage features are fed into *Decoder* for final semantic segmentation.

a combination of some of those images to generate high-resolution LF images. Moreover, AIFLFNet [63] utilized LF images to estimate depth information. Additionally, SAA-Net [64] introduces spatial-angular attention modules for LF image reconstruction. Especially, a design from [65] proposes a unified block for handling macro-pixel images, which can be used for both super-resolution and disparity estimation. Furthermore, [66] has also implemented LF technology for image reconstruction in the autonomous community.

For light-field semantic segmentation, the work of [16] utilizes stacks of sub-aperture images from certain directions, achieving the segmentation of central-view images. LFIE-Net [19] introduces an explicit branch to generate disparity maps within the network and cooperates with the sub-aperture images to achieve dense semantic segmentation. Specifically, multiple applications of LF technology in autonomous vehicles have been introduced, showing promising performance.

However, the high resolution of LF images presents a significant challenge due to memory costs for these methods. Unlike existing works, our proposed OAFuser has the capability to handle an arbitrary number of sub-aperture images without the demand for increased parameters in the context of light-field road-scene semantic understanding.

### III. METHODOLOGY

This section provides a detailed introduction to our proposed network, *i.e.*, *Omni-Aperture Fuser (OAFuser)*, which is tailored for LF semantic segmentation. The overall OAFuser architecture is presented in Sec. III-A. The *Sub-Aperture Fusion Module (SAFM)* for light-field feature aggregation is introduced in Sec. III-B. The *Center Aperture Rectification Module (CARM)* is in Sec. III-C.

#### A. Proposed OAFuser Architecture

As shown in Fig. 3, the proposed OAFuser is constructed with a four-stage encoder and a decoder. The encoder consists of the proposed SAFM and CARM to handle the feature fusion, feature embedding, and feature rectification, respectively. For simplicity, the following description is based on stage one, which is the same for the other three stages. Especially, the arbitrary number of LF images is described as sub-aperture images  $F_{s_i} \in \mathbb{R}^{H \times W \times 3}$  and central view image  $F_c \in \mathbb{R}^{H \times W \times 3}$ , where  $s_i$  is the  $i$ -th sub-aperture image in range  $[1, N]$ . All of them are fed into SAFM to embed angular feature  $F_{agl} \in \mathbb{R}^{\frac{H}{8} \times \frac{W}{8} \times 64}$  that contains rich angular information and spatial feature  $F_{spl} \in \mathbb{R}^{\frac{H}{8} \times \frac{W}{8} \times 64}$  which focus on spatial information for the central view. By applying two different transformer blocks following [12], both of the features transformed into  $F_{agl}^* \in \mathbb{R}^{\frac{H}{8} \times \frac{W}{8} \times 64}$  and  $F_{spl}^* \in \mathbb{R}^{\frac{H}{8} \times \frac{W}{8} \times 64}$ . After that, the angular and spatial features are concatenated for the next CARM, which includes Horizontal Operation and Vertical Operation for feature rectification along the horizon and vertical direction to eliminate asymmetry. Specially, the concatenation of  $F_{spl}^*$  and  $F_{agl}^*$  along the horizon direction is applied to obtain  $F_{c1} \in \mathbb{R}^{\frac{H}{8} \times \frac{W}{4} \times 64}$ . After the Global Rectification and Local Rectification, the horizontally rectified feature  $F^H \in \mathbb{R}^{2 \times \frac{H}{8} \times \frac{W}{8} \times 64}$  is obtained. Then, given the feature  $F^H$ , the feature  $F_{c2} \in \mathbb{R}^{\frac{H}{4} \times \frac{W}{8} \times 64}$  is obtained by the operation of disentanglement and concatenation along the vertical direction. Especially,  $F^H \in \mathbb{R}^{2 \times \frac{H}{8} \times \frac{W}{8} \times 64}$  is disentangled into  $F_{agl}^H \in \mathbb{R}^{\frac{H}{8} \times \frac{W}{8} \times 64}$  and  $F_{spl}^H \in \mathbb{R}^{\frac{H}{8} \times \frac{W}{8} \times 64}$ .  $F_{agl}^H$  and  $F_{spl}^H$  are further concatenated along vertical direction. After applying Global Rectification and Local Rectification in Vertical Operation, the rectified features  $F^G \in \mathbb{R}^{2 \times \frac{H}{8} \times \frac{W}{8} \times 64}$ .  $F_{agl}^G \in \mathbb{R}^{\frac{H}{8} \times \frac{W}{8} \times 64}$  and  $F_{spl}^G \in \mathbb{R}^{\frac{H}{8} \times \frac{W}{8} \times 64}$  is obtained by disentanglement of  $F^G$ . Furthermore, those two rectified features,

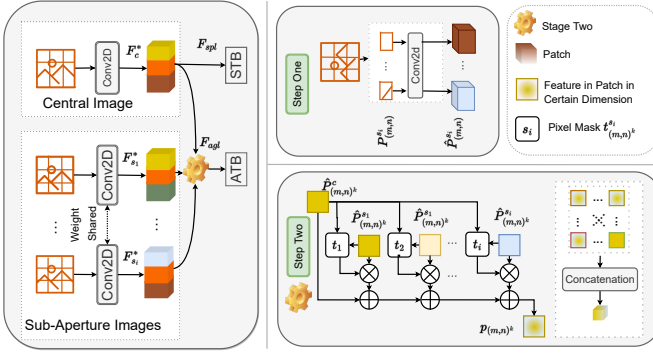


Fig. 4: **The structure of the Sub-Aperture Fusion Module (SAFM).** It consists of two stages. Given  $N + 1$  images, which include  $N$  sub-aperture images and one central view image, are conducted in SAFM. SAFM embeds the rich information into angular feature  $F_{agl}$  and Spatial Feature  $F_{spl}$ .  $STB$  and  $ATB$  denote Spatial Transformer Block and Angular Transformer Block respectively.

i.e.,  $F_{agl}^G$  and  $F_{spl}^G$  are fused by using the FFM module [12], which integrates two different features, to produce the final feature  $f_1$  for this stage. The weights between Horizontal Operation and Vertical Operation are shared.

Note that one of our crucial designs is *all sub-aperture information is fed into each stage*, which allows our network to consider all the sub-aperture images throughout the entire process effectively. The pyramidal features  $f_1, f_2, f_3, f_4$  are obtained via the four-stage encoder in a dimension of  $\{64, 128, 320, 512\}$ . Afterward, the multi-stage features are further fed into MLP Decoder [7] for final prediction.

### B. Sub-Aperture Fusion Module

To retrieve the rich angular and spatial information from LF images, we introduce the SAFM module, which embeds that information into angular and spatial features. As shown in Fig. 4, the SAFM consists of two steps. The first step of our SAFM is to extract features from all the LF images. All images are firstly divided into patches  $P_{(m,n)}^{s_i}, P_{(m,n)}^c$ , correspondence to sub-aperture images  $F_{s_i}$  and  $F_c$ , and further fed into the convolutional layer to extract features, resulting in  $\hat{P}_{(m,n)}^{s_i}$  and  $\hat{P}_{(m,n)}^c$ , where  $m, n$  denotes the relative position of the patch in a single feature map. The patch size follows [12]. Especially, our work aims to segment the central view image. Thus, the weights for the center view are performed individually, which ensures the spatial information of the central view remains independent. The weights for sub-aperture images are shared between different sub-aperture images. The calculations are presented in Eq. (1) and Eq. (2):

$$\hat{P}_{(m,n)}^{s_i} = \text{Conv}^{sub}(C_{in}, C_{out})(P_{(m,n)}^{s_i}), \quad (1)$$

$$\hat{P}_{(m,n)}^c = \text{Conv}^{cen}(C_{in}, C_{out})(P_{(m,n)}^c), \quad (2)$$

where  $\text{Conv}(C_{in}, C_{out})$  means the convolutional layer with input dimension  $C_{in}$  and output dimension  $C_{out}$ . For the first stage,  $C_{in}$  is 3 and  $C_{out}$  is 64. After that, the central image features  $F_{spl}$  are obtained by combining different patches

$\hat{P}_{(m,n)}^c$  and fed into the Spatial Transformer Block (STB). Meanwhile, the patches of the central view are also fed into the next step to cooperate with patches of the sub-aperture image to obtain angular features.

Afterward, the second step of SAFM is illustrated in Fig. 4, which is presented as the yellow gear symbol. For each patch  $\hat{P}_{(m,n)}^{s_i}$  of dimension  $k$ , the channel score  $e_{(m,n)}^{s_i}$  is calculated by obtaining the euclidean distance between each patch from the sub-aperture feature in dimension  $k$  and the corresponding patch from center view feature in dimension  $k$ , as in Eq. (3):

$$e_{(m,n)}^{s_i} = \text{Abs}(\hat{P}_{(m,n)}^c - \hat{P}_{(m,n)}^{s_i}), \quad (3)$$

where  $\text{Abs}(\cdot)$  denotes absolute value between two patch in channel  $k$ . Given the  $e_{(m,n)}^{s_i}$ , the mask score  $t_{(m,n)}^{s_i}$  for  $\hat{P}_{(m,n)}^{s_i}$  is obtained by mapping into the range of  $[1,0]$  and squaring them to enhance the discrimination, as shown in Eq. (4).

$$t_{(m,n)}^{s_i} = (\Theta\{e_{(m,n)}^{s_i}\})^2, \quad (4)$$

where  $\Theta\{\cdot\}$  denotes mapping operation. After obtaining the mask scores, the certain patch  $P_{(m,n)}^k$  of angular feature can be calculated. To be more detailed, the patch  $P_{(m,n)}^k$  in angular feature  $F_{agl}$  at position  $(m, n)$  in channel  $k$  can be calculated by summarizing the corresponding central view patch  $\hat{P}_{(m,n)}^c$  with masked sub-aperture patches  $\hat{P}_{(m,n)}^{s_i}$ , as in Eq. (5).

$$P_{(m,n)}^k = \hat{P}_{(m,n)}^c + \sum_{i=1}^N t_{(m,n)}^{s_i} \cdot \hat{P}_{(m,n)}^{s_i}. \quad (5)$$

Finally, the patch of angular feature  $P_{(m,n)}$  is obtained by concatenation of  $P_{(m,n)}^k$  as in Eq. (6). The angular feature  $F_{agl}$  is filled by  $P_{(m,n)}$  and further fed into Angular Transformer Block (AFB).

$$P_{(m,n)} = \text{Concat}(P_{(m,n)}^k). \quad (6)$$

### C. Central Angular Rectification Module

To eliminate information asymmetry, the CARM is a crucial design to rectify both spatial and angular features while simultaneously rearranging the features captured from different viewpoints. As shown in Fig. 5, two features from different transformer blocks are fed into CARM, which includes Horizontal and Vertical Operations. Since the Horizontal and Vertical Operations are symmetrical, only the Horizontal Operation is introduced in detail. In each operation, Global Rectification and Local Rectification are applied to rectify feature cues in different regions. At the end of CARM, the two features  $F_{agl}^G$  and  $F_{spl}^G$ , which correspond to  $F_{agl}^*$  and  $F_{spl}^*$ , are further fed into FFM (Feature Fusion Module). Specifically, in the Horizontal Operation,  $F_{agl}^*$  and  $F_{spl}^*$  is first concatenated along horizontal direction into feature  $F_{c1} \in \mathbb{R}^{\frac{H}{8} \times \frac{W}{4} \times 64}$ . To intuitively represent the dimension change between different steps, we use  $F_{c1} \in \mathbb{R}^{H \times 2W \times C_1}$  as the concatenated feature.  $F_{c1}$  is firstly fed into the **Global Rectification** stage. By applying an embedding process,  $F_{c1}$  is projected into  $F_{c1}^* \in \mathbb{R}^{H \times 2W \times C_2}$ ,

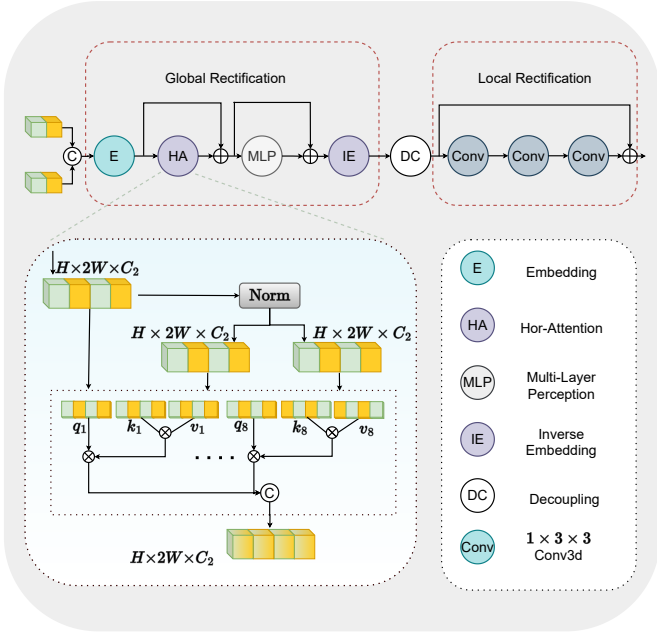


Fig. 5: The structure of Horizontal Operation in Center Angular Rectification Module (CARM). It consists of Global Operation and Local Operation.

which contain a set of tokens  $T_{c1}^* \in \mathbb{R}^{2W \times C_2}$ , with the projection matrix  $M_{in} \in \mathbb{R}^{C_1 \times C_2}$ , where  $C_1$  denotes the input dimension of features, and  $C_2$  denotes the embedding dimension for each token, the number of tokens is  $2W$ . To mitigate the covariate shift,  $\hat{T}_{c1}^* \in \mathbb{R}^{H \times 2W \times C_2}$  with tokens  $\dot{T}_{c1}^* \in \mathbb{R}^{2W \times C_2}$  is obtained by applying normalization of  $F_{c1}^*$ , following [35]. Then, the tokens, which represent the feature cues in a row, are utilized to generate query ( $Q$ ), key ( $K$ ), and value ( $V$ ). To be more specific,  $Q \in \mathbb{R}^{2W \times C_2}$  and  $K \in \mathbb{R}^{2W \times C_2}$  are obtained by multiplication of tokens  $\dot{T}_{c1}^*$  with matrices  $M_q \in \mathbb{R}^{C_2 \times C_2}$  and  $M_k \in \mathbb{R}^{C_2 \times C_2}$ , respectively. The matrix  $M_v \in \mathbb{R}^{C_2 \times C_2}$  multiplies the  $T_{c1}^*$  to generate  $V \in \mathbb{R}^{2W \times C_2}$ . Furthermore,  $Q$ ,  $K$ , and  $V$  are divided along the channel dimension and fed into eight heads. The similarity of each head can be calculated by dot product and followed by a Softmax function to obtain the similarity scores in each head between those tokens, as in Eq. (7).

$$\text{Similarity}_{head_1} = \text{Softmax} \frac{Q_i \cdot K_i^T}{\sqrt{D_i}}, i \in [1, 8]. \quad (7)$$

Based on the similarity scores, the rectified tokens  $T_{hi}^a$  in each head can be obtained by multiplying with  $V_i$ , as in Eq. (8).

$$T_{hi}^a = \text{Similarity}_{head_i} \cdot V_i, i \in [1, 8]. \quad (8)$$

The final tokens  $T_h^a \in \mathbb{R}^{2W \times C_2}$  are obtained by concatenation, as in Eq. (9).

$$T_h^a = \text{Concat}\{T_{h_1}^a, T_{h_2}^a, \dots, T_{h_8}^a\}. \quad (9)$$

Given the final tokens  $T_h^a$ , an MLP layer is adapted, and a linear layer is to project tokens into demotion  $C_1$ . The final

Dataset	Train	Val	Test	Total
UrbanLF-Real	580	80	164	824
UrbanLF-Syn	172	28	50	250
UrbanLF-RealE	780	80	164	1024

TABLE II: Statistic information of LF semantic segmentation datasets. UrbanLF-RealE denotes UrbanLF-Real with an extension of synthetic samples for training.

feature  $\overline{F}_h^a \in \mathbb{R}^{H \times 2W \times C_1}$  after Global Rectification can be formulated as in the Eq. (10),

$$\overline{F}_h^a = \text{LN}(C_2, C_1)(\text{MLP}(F_h^a) + F_h^a), \quad (10)$$

where  $\text{LN}(C_2, C_1)(\cdot)$  denotes linear projection.

By decoupling the feature  $\overline{F}_h^a$ , the rectified feature stack  $F_h^l \in \mathbb{R}^{2 \times H \times W \times C_1}$  is obtained. Furthermore, to further rectify the features in surrounding areas, the **Local Rectification** stage, which contains three convolutional layers, is implemented as in Eq. (12), where  $C$  denotes the input channel and output channel,  $\{\cdot\} \otimes 2$  denotes repeat those layers two times.

$$\hat{F}_h^l = \{\text{LReLU}(\text{Conv3D}(C, C)(F_h^l))\} \otimes 2, \quad (11)$$

$$F^H = \text{Conv3D}(C, C)(\hat{F}_h^l). \quad (12)$$

By disentangling of  $F^H \in \mathbb{R}^{2 \times H \times W \times C_1}$ ,  $F_{agl}^H \in \mathbb{R}^{H \times W \times C_1}$  and  $F_{spl}^H \in \mathbb{R}^{H \times W \times C_1}$  is obtained and further fed into Vertical Operation after concatenation.

## IV. EXPERIMENT RESULTS

### A. Datasets

Our experiments are based on the UrbanLF dataset [16]. The dataset comprises 14 categories for urban semantic scene understanding. Each sample in the dataset consists of 81 sub-aperture images with an angular resolution of  $9 \times 9$ . In our experiments, we follow the protocols proposed in UrbanLF and conducted three sets of experiments: Urban-Syn, Urban-Real, and UrbanLF-RealE. The UrbanLF-RealE is an extension of all real and synthetic data. Table II presents the number of images used for training, validation, and testing.

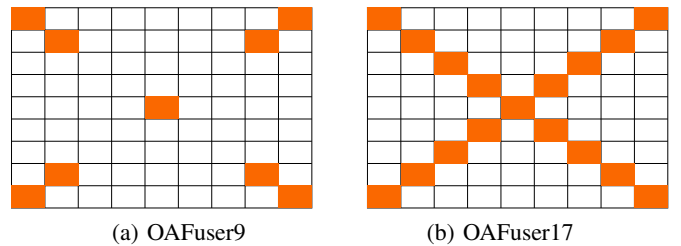


Fig. 6: The proposed selection strategy of light field images, i.e., OAFuser9 (left) and OAFuser17 (right).

Method	Type	Acc (%)	mAcc (%)	mIoU (%)
PSPNet [67]	RGB	91.21	83.87	76.34
DeepLabv3+ [27]	RGB	91.02	83.53	76.27
SETR [68]	RGB	92.16	84.27	77.74
OCR [69]	RGB	92.02	85.17	78.60
Accel [70]	Video	89.15	80.69	71.64
TDNet [71]	Video	91.05	83.38	76.48
DAVSS [20]	Video	91.04	83.54	75.91
TMANet [21]	Video	91.67	84.13	77.14
PSPNet-LF [16]	LF	92.14	84.86	78.10
OCR-LF [16]	LF	92.51	86.31	79.32
LF-IENet <sup>4</sup> [19]	LF	92.01	85.10	78.09
LF-IENet <sup>3</sup> [19]	LF	92.09	86.03	79.19
<b>OAFuser9</b>	LF	<b>94.45 (+1.94)</b>	<b>88.21 (+1.90)</b>	<b>82.69 (+3.37)</b>
<b>OAFuser17</b>	LF	94.08 (+1.52)	87.74 (+1.43)	82.21 (+2.89)

TABLE III: Quantitative results on the UrbanLF-Real dataset. Acc (%), mAcc (%), and mIoU (%) are reported. The best results are highlighted in red. The variation term indicates the performance difference from the previous best result.

### B. Implementation Details

The image size for UrbanLF-Syn is  $640 \times 480$  while applying zero padding converts samples in UrbanLF-Real into a size of  $640 \times 480$ . Data augmentation is applied with random flipping with a probability of 0.5, random scaling factors  $\{0.5, 0.75, 1, 1.25, 1.5, 1.75\}$ , normalization with mean factors  $\{0.485, 0.456, 0.406\}$ , and standard deviation factors  $\{0.229, 0.224, 0.225\}$ . We use the AdamW optimizer with momentum parameters  $\{0.9, 0.999\}$  and a weight decay of 0.01. The original learning rate is set to  $6e^{-5}$  and scheduled using the polynomial strategy with a power of 0.9. The first 10 epochs are used to warm up the models.

For experiments on the three different datasets, the training process adapts on three A40 GPUs with a batch size of 3 on each GPU and the number of training epochs is limited to a maximum of 500, and the model is based on the MiT-B4 per-train weight [7]. For the ablation study of architecture, we train our model with MiT-B2 [7] on one A5000 GPU with a batch size of 2 and epoch 200. With the MiT-B0 [7] on one A5000 GPU with a batch size of 2, we conduct an ablation study on the CARM and the investigation on the selection of sub-aperture images. For the selection of sub-aperture images, we choose images that are rich in angular information, mainly in the diagonal, as shown in Fig. 6. The experiments on the selection strategy of sub-aperture light-field images are discussed in Sec. V-E.

### C. Quantitative Results

To verify our methods, we compare OAFuser with other methods, which include RGB-based methods [27], [67], [68], [69], video-based light field semantic segmentation methods [20], [21], [70], [71], and several specific designs for light field semantic segmentation [16], [19] on three datasets, *i.e.*, UrbanLF-Real, UrbanLF-Syn, and UrbanLF-RealE.

Method	Type	Acc (%)	mAcc (%)	mIoU (%)
PSPNet [67]	RGB	89.39	84.48	75.78
SETR [68]	RGB	90.97	85.26	77.69
DeepLabv3+ [27]	RGB	89.60	83.55	75.39
OCR [69]	RGB	91.50	86.96	79.36
ACNet [39]	RGB-D	92.53	86.62	78.56
MTINet [4]	RGB-D	91.24	86.94	79.10
ESANet [43]	RGB-D	91.81	86.26	79.43
SA-Gate [15]	RGB-D	92.10	87.04	79.53
Accel [70]	Video	87.56	80.52	70.48
TDNet [71]	Video	89.06	83.43	74.71
DAVSS [20]	Video	89.47	82.94	74.27
TMANet [21]	Video	89.76	84.44	76.41
PSPNet-LF [16]	LF	90.55	85.91	77.88
OCR-LF [16]	LF	92.01	87.71	80.43
LF-IENet <sup>4</sup> [19]	LF	90.42	86.17	78.27
LF-IENet <sup>3</sup> [19]	LF	92.41	<b>88.31</b>	81.78
<b>OAFuser9</b>	LF	93.23 (+0.82)	88.26 (-0.05)	81.64 (-0.14)
<b>OAFuser17</b>	LF	<b>93.42 (+1.01)</b>	88.22 (-0.09)	<b>81.93 (+0.15)</b>

TABLE IV: Quantitative results on the UrbanLF-Syn dataset. Acc (%), mAcc (%), and mIoU (%) are reported. The best results are highlighted in red. The variation term indicates the performance difference from the previous best result.

1) *Results on UrbanLF-Real*: Table III presents the quantitative results on the UrbanLF-Real dataset, which is challenging due to issues like out-of-focus from the plenoptic camera and remaining consistency with LF camera implementation without further data pre-processing in real-world scenarios. Our OAFuser9 model achieves a state-of-the-art mIoU score of 82.69%, showing an improvement of 3.37% compared to previous methods. Similarly, our OAFuser17 model achieves a mIoU of 82.21%, with an increase of 2.89%. Regarding Acc and mAcc, our OAFuser9 and OAFuser17 have improved by over 1% compared to previous works. The small performance gap between our OAFuser9 and OAFuser17 is attributed to the image quality, which will be discussed in Sec. V-C.

As the quantity of sub-aperture images escalates, there emerges a proportional augmentation in the prevalence of extraneous features within the dataset. Furthermore, the prevalence of out-of-focus and blurry images has resulted in imprecise guidance, distinguishing our network from others. In our approach, we meticulously implement selective embedding of features during the feature integration phase. From another perspective, it also demonstrates the necessity of our correction module in handling semantic segmentation with LF cameras. The results clearly demonstrate the remarkable effectiveness of the suggested module structure and support our proposed approach, which leverages the rich angular information present in sub-aperture images and combines it with the spatial information from the central view. This fusion of data proves to be beneficial for accurately segmenting the central view image.

2) *Results on UrbanLF-Syn*: The quantitative results on the synthetic dataset are shown in Table IV. Among all the models assessed, OAFuser17 attains the highest mIoU. Comparatively,

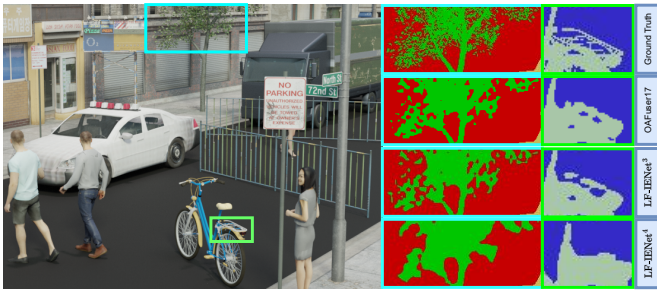


Fig. 7: Qualitative result for our network on the UrbanLF Syn dataset compared with LF-IENet [19].

OAFuser9 exhibits slightly inferior performance to LF-IENet<sup>3</sup>. This discrepancy in performance can be primarily attributed to the restricted size of the synthetic dataset, encompassing merely 173 samples for training purposes. In concrete terms, OAFuser makes use of the small differences present among different sub-aperture images to capture intricate angular details. These details are then combined with the appropriate spatial information obtained from the main viewpoint. This approach differs from previous methods that mainly focus on spatial information limited to the central view and overlook the angular information available from the LF camera. Additionally, a key feature of OAFuser is its ability to eliminate the need for pre-processing of initial LF images, showcasing its capability to handle raw LF data by effectively utilizing various angular information. Importantly, the network’s processing capabilities are not adequately demonstrated when using entirely focused images from synthetic datasets. Furthermore, it can be clearly seen from Fig. 7 in areas of complex structures, such as the leaves and bicycle pillion seats. Compared with LF-IENet, which leads to loss of global context for objects, such as the gaps between objects and their connection with branches being disrupted, our approach demonstrates better segmentation results even with 17 sub-aperture images. This underscores the superior capability of our network in harnessing sub-aperture images; through sophisticated rectification, the OAFuser consistently synchronizes with the rich tapestry of information gleaned from diverse perspectives. This claim has also been supported by experiments conducted on both the UrbanLF-Real and the UrbanLF-RealE datasets.

3) *Results on UrbanLF-RealE*: UrbanLF-RealE, which involves not only real-world samples but also extends to multiple synthetic samples, poses significant challenges to the performance of the model. This complex combination of data is more aligned with unconstrained scenarios. As shown in Table V, OAFuser achieves state-of-the-art performance with mIoU of 84.93%. The result exceeds all the existing methods by more than 4.53%. The accuracy of OAFuser17 decreases compared to OAFuser9, which is caused by the challenges posed by a large number of sub-aperture images in complex scenarios. Due to the increasing number of sub-aperture images, it becomes challenging to accurately distinguish between relevant and irrelevant features in a dataset where focused and defocused images are mixed together. Compared with PSPNet-LF and OCR-LF, which implement the direct fusion of sub-

Method	Type	Acc (%)	mAcc (%)	mIoU (%)
PSPNet [67]	RGB	91.73	84.47	77.71
DeepabV3+ [27]	RGB	91.33	83.86	76.70
SETR [68]	RGB	92.72	85.55	79.06
OCR [69]	RGB	92.56	86.56	79.90
Accel [70]	Video	89.40	82.30	72.85
TDNet [71]	Video	91.48	84.25	77.52
DAVSS [20]	Video	91.96	85.21	77.31
TMANet [21]	Video	91.84	84.81	78.13
PSPNet-LF [16]	LF	92.69	86.01	79.45
OCR-LF [16]	LF	92.95	86.94	80.40
<b>OAFuser9</b>	LF	<b>94.61 (+1.66)</b>	<b>89.84 (+2.90)</b>	<b>84.93 (+4.53)</b>
<b>OAFuser17</b>	LF	93.74 (+0.79)	88.92 (+1.98)	82.42 (+2.02)

TABLE V: Quantitative results on the UrbanLF-RealE dataset. Acc (%), mAcc (%), and mIoU (%) are reported. The best results are highlighted in red. The variation term indicates the performance difference from the previous best result.

aperture and central-view images, our OAFuser embeds the rich angular feature in an independent branch and focuses on utilizing both spatial and angular features.

Above all, the excellent performance on the UrbanLF-RealE dataset demonstrates the superiority of our design and sets a new record of LF semantic segmentation. The network showcases remarkable accuracy without relying on extensive image preprocessing and additional devices. This validates the applicability of our network in real-world scenarios.

## V. ABLATION STUDIES

In this section, we conduct several ablation studies to confirm the impact of different modules in our proposed method and to demonstrate the contribution of various sub-aperture images from the light field camera to the understanding of the urban scene. The experiments are carried out in Sec. V-A to thoroughly investigate the effects of diverse components incorporated in our method. Additionally, we conduct several experiments in Sec. V-B to determine the optimal combination in the CARM. Furthermore, we compare the impact of different datasets in Sec. V-C and analyze the per-class performance in Sec. V-D. Moreover, the exploration of the contributions of sub-aperture images is conducted in Sec. V-E.

### A. Ablation Study for the Overall Model

As shown in Table VI, we ablate our OAFuser structure gradually. When removing the CARM and replacing it with the Feature Rectification Module (FRM) [12]. The accuracy dramatically decreases by 2.17%. Although the number of parameters is also reduced, our CARM module is essential to overcome challenges such as image mismatching and out-of-focus issues. Besides, we ablate the components of SAFM progressively, *i.e.*, using SAFM in the first or last stage, and without SAFM. The performances of these three variants

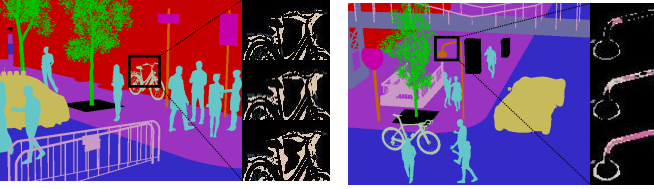


Fig. 8: Visualization of the proposed architecture. From top to bottom are the entire OAFuser model, OAFuser without CARM, and OAFuser without CARM and SAFM.

are decreased significantly (2~3% drops compared to OAFuser). Especially notably in these variants, the number of parameters remains unchanged, as the angle information is obtained through channel-level feature aggregation with shared weights. This also validates that the introduction of the SAFM efficiently achieves the selection and fusion of rich information from the LF camera, and the network has the capability to handle arbitrary sub-aperture images. Furthermore, the FFM [12] is also essential since combining complementary features is crucial in the LF semantic segmentation task.

Moreover, we conduct visualization comparisons in this ablation study. Fig. 8 illustrates the difference maps of the cropped region compared to the ground-truth mask, which is generated by the overall OAFuser model, the one without CARM and the other without CARM and SAFM, respectively. The visualization result indicates the effectiveness of using CARM and SAFM for light-field semantic segmentation.

### B. Ablation Study for CARM

To rigorously assess the efficacy of our proposed method for rectifying asymmetric features, we embarked on a comprehensive suite of ablation studies centered around the innovative CARM framework. As depicted in Table VIIa, we remove the local rectification module and increase the embedding dimension of the global module from  $C$  to  $4C$  to assess the optimal manner. Subsequently, upon projecting the dimensions to  $2C$ , our network achieves the highest score of 72.87%. Besides, excessively large dimensions ( $>2C$ ) might hinder the capacity to parse the features. To address the issue, we further explore the number of layers of 3D convolution in Local Rectification to evaluate the impact. As in Table VIIb, the employment of 3D convolutions proves advantageous for feature rectification when the number of convolutional layers is  $<4$ , and the best mIoU peaks at 73.39%. However, when

Model	#Params(M)	mIoU(%)
OAFuser (ours)	79.2	77.18
- Without CARM	65.0 (-14.2)	75.01 (-2.17)
- SAFM only at Stage One	65.0 (-14.2)	73.50 (-3.68)
- SAFM only at Stage Four	65.0 (-14.2)	73.46 (-3.72)
- Without SAFM	65.0 (-14.2)	73.25 (-3.93)
- Without FFM	58.4 (-20.8)	70.25 (-6.93)

TABLE VI: Ablation study of the OAFuser framework.

Dimension	C	2C	3C	4C	5C
mIoU	70.55	<b>72.87</b>	71.52	71.93	70.57

(a) Exploration of the embedding dimension in Global Rectification. The *Dimension* denotes embedding dimension.

Layers	0	1	2	3	4	P
mIoU	72.87	73.13	73.06	<b>73.39</b>	71.49	61.49

(b) Exploration of Local Rectification. **P** denotes the parallel addition of features from both groups.

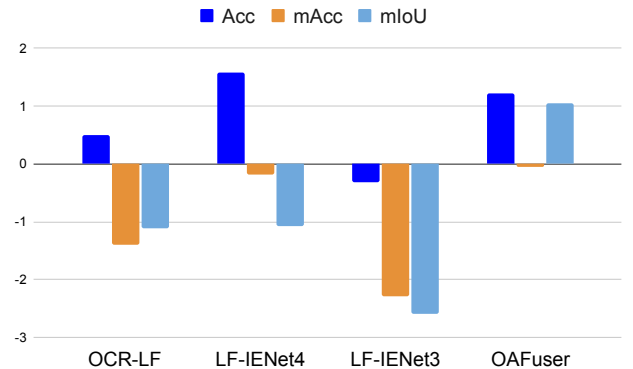
TABLE VII: Ablation Study of the Central Angular Rectification Module (CARM). *Dimension* denotes the embedding dimension in Global Operation, and *Layers* presents the number of 3D convolutions within Local Operation. mIoU (%) is reported. The best results are highlighted in red.

utilizing four layers of 3D convolutions, the interconnections between different features are significantly disrupted, leading to a diminished mIoU score of 71.49%.

Subsequently, after exploring the combination of the Local Rectification Module and the Global Rectification Module through the parallel addition of features from both, it was observed that there was a degradation in the network's discriminative capability. This unexpected outcome also proves the effectiveness of our network.

### C. Dataset Comparison

To further prove the performance of our network, we analyze the impact of image quality among distinct datasets. While the number of classes and their distribution exhibit similarity across the datasets, the most prominent difference lies in the image quality, as expounded in UrbanLF [16].



Model	OCR-LF	LF-IENet4	LF-IENet3	OAFuser
Acc	0.50	<b>1.59</b>	-0.32	1.22
mAcc	-1.40	-0.18	-2.28	<b>-0.05</b>
mIoU	-1.11	-1.07	-2.59	<b>1.05</b>

Fig. 9: The performance comparison between different networks. Acc (%), mAcc (%), and mIoU (%) are reported. The best results are highlighted in red.

Dataset	Method	IoU														Acc	mAcc	mIoU
		Bike	Building	Fence	Others	Person	Pole	Road	Sidewalk	Traffic Sign	Vegetation	Vehicle	Bridge	Rider	Sky			
RealE	Proportion	2.27	33.48	3.86	1.59	3.08	1.42	21.36	8.00	0.65	3.05	16.46	2.34	0.24	2.19	n.a.	n.a.	n.a.
	CMX MiT-B4	86.88	90.52	76.27	43.47	91.31	73.47	90.74	68.70	86.22	85.21	96.45	74.33	69.15	96.61	93.00	87.00	80.66
	OAFuser9	87.92	91.95	87.64	48.56	93.63	77.55	91.74	71.92	87.43	89.04	97.05	88.89	79.03	96.61	94.61	89.84	<b>84.93 (+4.55)</b>

TABLE VIII: Per-class statistics of CMX and OAFuser on the UrbanLF-RealE dataset are presented. *Proportion* represents the class percentage, and the values are given in percentage (%). The best result is highlighted in red.

As shown in Fig 9, the presence of noise in out-of-focus images leads to performance degradation for LF-IENet<sup>3</sup>, LF-IENet<sup>4</sup>, and OCR-LF, resulting in a decline of more than 1% in mIoU. However, the mIoU score of our OAFuser increases by 1.05%. This improvement contributes to the proposed method and the design of our model, which leverages abundant angular information and rectifies features from various viewpoints, consequently reducing the impact of image quality on our model. For existing works, the improved accuracy values and decreased mAcc also demonstrate the challenges posed by the quality in distinguishing different class boundaries. However, while improving classification accuracy, our model shows a minimal decrease in mAcc (-0.05%).

#### D. Per-Class Accuracy Analysis

To comprehensively assess the model’s performance per class and delve deeper into the improvement achieved by our model in comparison with the baseline method, we present a summary of statistical information from different methods in Table VIII. Moreover, the class proportion assisting in data analysis is also introduced.

Given that our baseline method, CMX [12], is designed for two modalities, we first aggregate the sub-aperture images before feeding them into the network. It can be seen that OAFuser significantly outperforms the baseline method across various categories, such as *fence*, *pole*, *sidewalk*, *vehicle*, *bridge* and *rider*, which are crucial for the road system in urban scenarios. Significantly, the recognition capability for *vehicle* even exceeds 97% in IoU.

Those results prove the achievement of our proposed model for segmentation tasks in urban scenes. By incorporating SAFM and CARM, the network unleashes the potential of the angle information from different sub-aperture images and leverages the consistency of variations among sub-aperture images. This enables OAFuser to deliver promising performance.

#### E. Investigation on the Selection of Sub-Aperture Images

To demonstrate that a more significant number of sub-aperture images, as compared to a single image, can provide more effective information for scene understanding, several experiments are conducted. As shown in Table IX, compared with our baseline method CMX [12], which is designed for similar modalities fusion, our OAFuser achieves an increase of more than 2% in mIoU. This result further confirms the effectiveness of our design in handling asymmetric data

Method	mIoU	Improvement
CMX MiT-B0 (RGB V11) [12]	68.40	
OAFuser2 MiT-B0	71.17	+2.77
OAFuser5 MiT-B0	71.92	+3.52
OAFuser9 MiT-B0	72.57	+4.17
OAFuser13 MiT-B0	72.60	+4.20
OAFuser17 MiT-B0	<b>72.87</b>	+4.47
OAFuser21 MiT-B0	72.22	+3.82
OAFuser17 MiT-B4	<b>81.93</b>	+13.53

TABLE IX: Exploration of the contribution of different numbers of sub-aperture images. mIoU (%) is reported. V11 denotes the sub-aperture image from the top-left viewpoint. The best results are highlighted in red.

from the LF camera for segmentation tasks. Furthermore, our network perceives the scene from multiple perspectives, and with increased viewpoints, it achieves progressively higher accuracy. This also showcases our network’s capacity to harness angular information and underscores the importance of leveraging a higher count of sub-aperture images for the segmentation task. Moreover, under the same model, the performance continually improves with the incremental addition of sub-aperture images, further validating the efficacy of sub-aperture images’ extraction and utilization in enhancing road scene understanding. OAFuser reaches its peak at OAFuser17.

## VI. CONCLUSION

In this paper, we explore the potential of light field cameras for road scene understanding with semantic segmentation. We propose a new, innovative paradigm, the Omni-Aperture Fusion (OAFuser), to exploit dense context and angular information from light field apertures effectively. We introduce the Sub-Aperture Fusion Module (SAFM), which enables the network to embed angular information from light field cameras without additional memory costs and ensures the feature consistency of angular features. With the Center Angular Rectification Module (CARM), our network enables the utilization of asymmetric features from different viewpoints. OAFuser sets state-of-art performance compared with existing works on three UrbanLF datasets. The proposed framework breaks the limitation introduced by redundant data and establishes a new baseline for the further exploration of LF.

In the future, we strive to establish a new benchmark with more categories and a larger set of training samples to assess the accuracy of using light field cameras for multiple scenarios.

Furthermore, the plan of visiting other computer vision tasks based on light field cameras is essential, since the application of light field cameras in visual tasks is still an under-explored domain. Summarily, we hope to inspire more interest in light field cameras and advance their development in computer vision community.

## REFERENCES

- [1] Z. Lu, R. Cheng, S. Huang, H. Zhang, C. Qiu, and F. Yang, "Surrogate-assisted multiobjective neural architecture search for real-time semantic segmentation," *IEEE Transactions on Artificial Intelligence*, vol. 4, no. 6, pp. 1602–1615, 2023.
- [2] S. Mazhar, N. Atif, M. Bhuyan, and S. R. Ahamed, "Rethinking DABNet: Light-weight network for real-time semantic segmentation of road scenes," *IEEE Transactions on Artificial Intelligence*, 2023.
- [3] Y. Liu, W. Zhang, G. Zhao, J. Zhu, A. V. Vasilakos, and L. Wang, "Test-time adaptation for nighttime color-thermal semantic segmentation," *IEEE Transactions on Artificial Intelligence*, 2023.
- [4] S. Vandenhende, S. Georgoulis, and L. Van Gool, "MTI-Net: Multi-scale task interaction networks for multi-task learning," in *European Conference on Computer Vision (ECCV)*, vol. 12349, 2020, pp. 527–543.
- [5] M.-H. Guo, C.-Z. Lu, Q. Hou, Z. Liu, M.-M. Cheng, and S.-M. Hu, "SegNeXt: Rethinking convolutional attention design for semantic segmentation," in *Advances in Neural Information Processing Systems (NeurIPS)*, vol. 35, 2022, pp. 1140–1156.
- [6] I. O. Tolstikhin *et al.*, "MLP-Mixer: An all-MLP architecture for vision," in *Advances in Neural Information Processing Systems (NeurIPS)*, vol. 34, 2021, pp. 24261–24272.
- [7] E. Xie, W. Wang, Z. Yu, A. Anandkumar, J. M. Alvarez, and P. Luo, "SegFormer: Simple and efficient design for semantic segmentation with transformers," in *Advances in Neural Information Processing Systems (NeurIPS)*, vol. 34, 2021, pp. 12077–12090.
- [8] Q. Zhang, Y. Xu, J. Zhang, and D. Tao, "VSA: Learning varied-size window attention in vision transformers," in *European Conference on Computer Vision (ECCV)*, vol. 13685, 2022, pp. 466–483.
- [9] Z. Zhang, X. Zhang, C. Peng, X. Xue, and J. Sun, "ExFuse: Enhancing feature fusion for semantic segmentation," in *European Conference on Computer Vision (ECCV)*, vol. 11214, 2018, pp. 273–288.
- [10] R. Zhang, S. A. Candra, K. Vetter, and A. Zakhor, "Sensor fusion for semantic segmentation of urban scenes," in *2015 IEEE International Conference on Robotics and Automation (ICRA)*, 2015, pp. 1850–1857.
- [11] C. Hazirbas, L. Ma, C. Domokos, and D. Cremers, "FuseNet: Incorporating depth into semantic segmentation via fusion-based CNN architecture," in *Asian Conference on Computer Vision (ACCV)*, vol. 10111, 2017, pp. 213–228.
- [12] J. Zhang, H. Liu, K. Yang, X. Hu, R. Liu, and R. Stiefelhagen, "CMX: Cross-modal fusion for RGB-X semantic segmentation with transformers," *IEEE Transactions on Intelligent Transportation Systems*, 2023.
- [13] T. Georgiev and C. Intwala, "Light field camera design for integral view photography," *Adobe System, Inc., Technical Report*, p. 1, 2006.
- [14] M. Meilland, A. I. Comport, and P. Rives, "Dense omnidirectional RGB-D mapping of large-scale outdoor environments for real-time localization and autonomous navigation," *Journal of Field Robotics*, vol. 32, no. 4, pp. 474–503, 2015.
- [15] X. Chen *et al.*, "Bi-directional cross-modality feature propagation with separation-and-aggregation gate for RGB-D semantic segmentation," in *European Conference on Computer Vision (ECCV)*, vol. 12356, 2020, pp. 561–577.
- [16] H. Sheng, R. Cong, D. Yang, R. Chen, S. Wang, and Z. Cui, "UrbanLF: A comprehensive light field dataset for semantic segmentation of urban scenes," *IEEE Transactions on Circuits and Systems for Video Technology*, vol. 32, no. 11, pp. 7880–7893, 2022.
- [17] T. Leistner, R. Mackowiak, L. Ardizzone, U. Köthe, and C. Rother, "Towards multimodal depth estimation from light fields," in *2022 IEEE/CVF Conference on Computer Vision and Pattern Recognition (CVPR)*, 2022, pp. 12943–12951.
- [18] W. Yan, X. Zhang, H. Chen, C. Ling, and D. Wang, "Light field depth estimation based on channel attention and edge guidance," in *2022 China Automation Congress (CAC)*, 2022, pp. 2595–2600.
- [19] R. Cong, D. Yang, R. Chen, S. Wang, Z. Cui, and H. Sheng, "Combining implicit-explicit view correlation for light field semantic segmentation," in *2023 IEEE/CVF Conference on Computer Vision and Pattern Recognition (CVPR)*, 2023, pp. 9172–9181.
- [20] J. Zhuang, Z. Wang, and B. Wang, "Video semantic segmentation with distortion-aware feature correction," *IEEE Transactions on Circuits and Systems for Video Technology*, vol. 31, no. 8, pp. 3128–3139, 2021.
- [21] H. Wang, W. Wang, and J. Liu, "Temporal memory attention for video semantic segmentation," in *2021 IEEE International Conference on Image Processing (ICIP)*, 2021, pp. 2254–2258.
- [22] D. G. Dansereau, O. Pizarro, and S. B. Williams, "Decoding, calibration and rectification for lenselet-based plenoptic cameras," in *2013 IEEE Conference on Computer Vision and Pattern Recognition (CVPR)*, 2013, pp. 1027–1034.
- [23] Y. Bok, H.-G. Jeon, and I. S. Kweon, "Geometric calibration of micro-lens-based light field cameras using line features," *IEEE Transactions on Pattern Analysis and Machine Intelligence*, vol. 39, no. 2, pp. 287–300, 2017.
- [24] W. Zhou, S. Dong, J. Lei, and L. Yu, "MTANet: Multitask-aware network with hierarchical multimodal fusion for RGB-T urban scene understanding," *IEEE Transactions on Intelligent Vehicles*, vol. 8, no. 1, pp. 48–58, 2023.
- [25] J. Zhang, K. Yang, A. Constantinescu, K. Peng, K. Müller, and R. Stiefelhagen, "Trans4Trans: Efficient transformer for transparent object and semantic scene segmentation in real-world navigation assistance," *IEEE Transactions on Intelligent Transportation Systems*, vol. 23, no. 10, pp. 19173–19186, 2022.
- [26] J. Long, E. Shelhamer, and T. Darrell, "Fully convolutional networks for semantic segmentation," in *2015 IEEE Conference on Computer Vision and Pattern Recognition (CVPR)*, 2015, pp. 3431–3440.
- [27] L.-C. Chen, Y. Zhu, G. Papandreou, F. Schroff, and H. Adam, "Encoder-decoder with atrous separable convolution for semantic image segmentation," in *European Conference on Computer Vision (ECCV)*, vol. 11211, 2018, pp. 833–851.
- [28] V. Badrinarayanan, A. Kendall, and R. Cipolla, "SegNet: A deep convolutional encoder-decoder architecture for image segmentation," *IEEE Transactions on Pattern Analysis and Machine Intelligence*, vol. 39, no. 12, pp. 2481–2495, 2017.
- [29] M. Yang, K. Yu, C. Zhang, Z. Li, and K. Yang, "DenseASPP for semantic segmentation in street scenes," in *2018 IEEE Conference on Computer Vision and Pattern Recognition (CVPR)*, 2018, pp. 3684–3692.
- [30] H. Ding, X. Jiang, B. Shuai, A. Q. Liu, and G. Wang, "Context contrasted feature and gated multi-scale aggregation for scene segmentation," in *2018 IEEE Conference on Computer Vision and Pattern Recognition (CVPR)*, 2018, pp. 2393–2402.
- [31] J. He, Z. Deng, L. Zhou, Y. Wang, and Y. Qiao, "Adaptive pyramid context network for semantic segmentation," in *2019 IEEE/CVF Conference on Computer Vision and Pattern Recognition (CVPR)*, 2019, pp. 7519–7528.
- [32] G. Lin, A. Milan, C. Shen, and I. Reid, "RefineNet: Multi-path refinement networks for high-resolution semantic segmentation," in *2017 IEEE Conference on Computer Vision and Pattern Recognition (CVPR)*, 2017, pp. 5168–5177.
- [33] J. Fu *et al.*, "Dual attention network for scene segmentation," in *2019 IEEE/CVF Conference on Computer Vision and Pattern Recognition (CVPR)*, 2019, pp. 3146–3154.
- [34] W. Wang, T. Zhou, F. Yu, J. Dai, E. Konukoglu, and L. Van Gool, "Exploring cross-image pixel contrast for semantic segmentation," in *2021 IEEE/CVF International Conference on Computer Vision (ICCV)*, 2021, pp. 7283–7293.
- [35] A. Dosovitskiy *et al.*, "An image is worth 16x16 words: Transformers for image recognition at scale," in *International Conference on Learning Representations (ICLR)*, 2021.
- [36] M. Sandler, A. Howard, M. Zhu, A. Zhmoginov, and L.-C. Chen, "MobileNetV2: Inverted residuals and linear bottlenecks," in *2018 IEEE Conference on Computer Vision and Pattern Recognition (CVPR)*, 2018, pp. 4510–4520.
- [37] M. Tan and Q. Le, "EfficientNet: Rethinking model scaling for convolutional neural networks," in *International Conference on Machine Learning (ICML)*, 2019, pp. 6105–6114.
- [38] X. Zhang, X. Zhou, M. Lin, and J. Sun, "ShuffleNet: An extremely efficient convolutional neural network for mobile devices," in *2018 IEEE Conference on Computer Vision and Pattern Recognition (CVPR)*, 2018, pp. 6848–6856.
- [39] X. Hu, K. Yang, L. Fei, and K. Wang, "ACNet: Attention based network to exploit complementary features for RGBD semantic segmentation,"

- in *2019 IEEE International Conference on Image Processing (ICIP)*, 2019, pp. 1440–1444.
- [40] J. Zhang, K. Yang, and R. Stiefelwagen, “Exploring event-driven dynamic context for accident scene segmentation,” *IEEE Transactions on Intelligent Transportation Systems*, vol. 23, no. 3, pp. 2606–2622, 2022.
- [41] H. Chen *et al.*, “MMFNet: A multi-modality MRI fusion network for segmentation of nasopharyngeal carcinoma,” *Neurocomputing*, vol. 394, pp. 27–40, 2020.
- [42] Z. Xing, L. Yu, L. Wan, T. Han, and L. Zhu, “NestedFormer: Nested modality-aware transformer for brain tumor segmentation,” in *International Conference on Medical Image Computing and Computer-Assisted Intervention (MICCAI)*, 2022, pp. 140–150.
- [43] D. Seichter, M. Köhler, B. Lewandowski, T. Wengefeld, and H.-M. Gross, “Efficient RGB-D semantic segmentation for indoor scene analysis,” in *2021 IEEE International Conference on Robotics and Automation (ICRA)*, 2021, pp. 13 525–13 531.
- [44] H. Mei *et al.*, “Glass segmentation using intensity and spectral polarization cues,” in *2022 IEEE/CVF Conference on Computer Vision and Pattern Recognition (CVPR)*, 2022, pp. 12 612–12 621.
- [45] Y. Sun, W. Zuo, and M. Liu, “RTFNet: RGB-thermal fusion network for semantic segmentation of urban scenes,” *IEEE Robotics and Automation Letters*, vol. 4, no. 3, pp. 2576–2583, 2019.
- [46] W. Zhou, J. Liu, J. Lei, L. Yu, and J.-N. Hwang, “GMNet: Graded-feature multilabel-learning network for RGB-thermal urban scene semantic segmentation,” *IEEE Transactions on Image Processing*, vol. 30, pp. 7790–7802, 2021.
- [47] Q. Ha, K. Watanabe, T. Karasawa, Y. Ushiku, and T. Harada, “MFNet: Towards real-time semantic segmentation for autonomous vehicles with multi-spectral scenes,” in *2017 IEEE/RSJ International Conference on Intelligent Robots and Systems (IROS)*, 2017, pp. 5108–5115.
- [48] J. Zhang *et al.*, “Delivering arbitrary-modal semantic segmentation,” in *2023 IEEE/CVF Conference on Computer Vision and Pattern Recognition (CVPR)*, 2023, pp. 1136–1147.
- [49] T. Broedermann, C. Sakaridis, D. Dai, and L. Van Gool, “HRFuser: A multi-resolution sensor fusion architecture for 2D object detection,” in *2023 IEEE International Conference on Intelligent Transportation Systems (ITSC)*, 2023.
- [50] L. Ruan, B. Chen, J. Li, and M. Lam, “Learning to deblur using light field generated and real defocus images,” in *2022 IEEE/CVF Conference on Computer Vision and Pattern Recognition (CVPR)*, 2022, pp. 16 283–16 292.
- [51] Y. Yang, L. Wu, L. Zeng, T. Yan, and Y. Zhan, “Joint upsampling for refocusing light fields derived with hybrid lenses,” *IEEE Transactions on Instrumentation and Measurement*, vol. 72, pp. 1–12, 2023.
- [52] A. Wang, M. Wang, X. Li, Z. Mi, and H. Zhou, “A two-stage bayesian integration framework for salient object detection on light field,” *Neural Processing Letters*, vol. 46, pp. 1083–1094, 2017.
- [53] J. Zhang, M. Wang, L. Lin, X. Yang, J. Gao, and Y. Rui, “Saliency detection on light field: A multi-cue approach,” *ACM Transactions on Multimedia Computing, Communications, and Applications (TOMM)*, vol. 13, no. 3, pp. 1–22, 2017.
- [54] K. Honauer, O. Johannsen, D. Kondermann, and B. Goldluecke, “A dataset and evaluation methodology for depth estimation on 4D light fields,” in *Asian Conference on Computer Vision (ACCV)*, vol. 10113, 2016, pp. 19–34.
- [55] J. Peng, Z. Xiong, Y. Wang, Y. Zhang, and D. Liu, “Zero-shot depth estimation from light field using a convolutional neural network,” *IEEE Transactions on Computational Imaging*, vol. 6, pp. 682–696, 2020.
- [56] Y. Wang, F. Liu, K. Zhang, G. Hou, Z. Sun, and T. Tan, “LFNet: A novel bidirectional recurrent convolutional neural network for light-field image super-resolution,” *IEEE Transactions on Image Processing*, vol. 27, no. 9, pp. 4274–4286, 2018.
- [57] J. Jin, J. Hou, J. Chen, and S. Kwong, “Light field spatial super-resolution via deep combinatorial geometry embedding and structural consistency regularization,” in *2020 IEEE/CVF Conference on Computer Vision and Pattern Recognition (CVPR)*, 2020, pp. 2257–2266.
- [58] G. Chen *et al.*, “Fusion-embedding siamese network for light field salient object detection,” *IEEE Transactions on Multimedia*, 2023.
- [59] M. Feng, K. Liu, L. Zhang, H. Yu, Y. Wang, and A. Mian, “Learning from pixel-level noisy label: A new perspective for light field saliency detection,” in *2022 IEEE/CVF Conference on Computer Vision and Pattern Recognition (CVPR)*, 2022, pp. 1746–1756.
- [60] Y. Wang, L. Wang, J. Yang, W. An, J. Yu, and Y. Guo, “Spatial-angular interaction for light field image super-resolution,” in *European Conference on Computer Vision (ECCV)*, vol. 12368, 2020, pp. 290–308.
- [61] Z. Liang, Y. Wang, L. Wang, J. Yang, S. Zhou, and Y. Guo, “Learning non-local spatial-angular correlation for light field image super-resolution,” *arXiv preprint arXiv:2302.08058*, 2023.
- [62] S. Zhang, Y. Lin, and H. Sheng, “Residual networks for light field image super-resolution,” in *2019 IEEE/CVF Conference on Computer Vision and Pattern Recognition (CVPR)*, 2019, pp. 11 046–11 055.
- [63] S. Zhou, L. Hu, Y. Wang, Z. Sun, K. Zhang, and X.-q. Jiang, “AIF-LFNet: All-in-focus light field super-resolution method considering the depth-varying defocus,” *IEEE Transactions on Circuits and Systems for Video Technology*, 2023.
- [64] G. Wu, Y. Wang, Y. Liu, L. Fang, and T. Chai, “Spatial-angular attention network for light field reconstruction,” *IEEE Transactions on Image Processing*, vol. 30, pp. 8999–9013, 2021.
- [65] Y. Wang *et al.*, “Disentangling light fields for super-resolution and disparity estimation,” *IEEE Transactions on Pattern Analysis and Machine Intelligence*, vol. 45, no. 1, pp. 425–443, 2023.
- [66] J. Casavilca Silva, M. Saadi, L. Wuttisittikulij, D. Ribeiro Militani, R. L. Rosa, D. Z. Rodríguez, and S. A. Otaibi, “Light-field imaging reconstruction using deep learning enabling intelligent autonomous transportation system,” *IEEE Transactions on Intelligent Transportation Systems*, vol. 23, no. 2, pp. 1587–1595, 2022.
- [67] H. Zhao, J. Shi, X. Qi, X. Wang, and J. Jia, “Pyramid scene parsing network,” in *2017 IEEE Conference on Computer Vision and Pattern Recognition (CVPR)*, 2017, pp. 6230–6239.
- [68] S. Zheng *et al.*, “Rethinking semantic segmentation from a sequence-to-sequence perspective with transformers,” in *2021 IEEE/CVF Conference on Computer Vision and Pattern Recognition (CVPR)*, 2021, pp. 6881–6890.
- [69] Y. Yuan, X. Chen, and J. Wang, “Object-contextual representations for semantic segmentation,” in *European Conference on Computer Vision (ECCV)*, vol. 12351, 2020, pp. 173–190.
- [70] S. Jain, X. Wang, and J. E. Gonzalez, “Accel: A corrective fusion network for efficient semantic segmentation on video,” in *2019 IEEE/CVF Conference on Computer Vision and Pattern Recognition (CVPR)*, 2019, pp. 8866–8875.
- [71] P. Hu, F. Caba, O. Wang, Z. Lin, S. Sclaroff, and F. Perazzi, “Temporally distributed networks for fast video semantic segmentation,” in *2020 IEEE/CVF Conference on Computer Vision and Pattern Recognition (CVPR)*, 2020, pp. 8815–8824.